Geometry-driven magnetization reversal and spin-wave dynamics in permalloy artificial anti–spin ice lattices

Szymon P. Oramus,[1] Riccardo Fornari,[2,3] Gianluca Gubbiotti,[3] and Adekunle O. Adeyeye[1,*]

[1]*Department of Physics, Durham University, Durham DH1 3LE, United Kingdom*
[2]*Dipartimento di Fisica e Geologia, Università di Perugia, Via A. Pascoli, 06123, Perugia, Italy*
[3]*CNR-Istituto Officina dei Materiali (IOM), 06123 Perugia, Italy*

(Received 14 July 2026; revised 7 October 2026; accepted 15 October 2026; published 6 November 2026)

Antiartificial spin ice (AASI), realized through spin-ice-derived antidot lattices of stadium-shaped holes in continuous Permalloy ($Ni_{81}Fe_{19}$) films, provides a powerful route for embedding geometry-induced magnetic anisotropy within a connected magnonic medium. Here, homogeneous and bicomponent AASI lattices are investigated through a combined experimental and micromagnetic approach, establishing a direct link between lattice geometry, magnetization reversal, and spin-wave (SW) dynamics. Magneto-optical Kerr effect measurements, Brillouin light scattering spectroscopy, and simulations reveal that antidot size, lattice heterogeneity, and magnetic field orientation collectively govern both equilibrium states and dynamic excitations. The static response exhibits pronounced angular anisotropy in coercivity and remanence, with bicomponent lattices showing distinct reversal pathways and shifted anisotropy extrema relative to homogeneous systems. These variations are directly reflected in the SW spectra, where edge-, node-, and domain-wall-localized modes, as well as mode splitting and frequency flattening, emerge as signatures of geometry-induced magnetization textures. The excellent agreement between experiment and simulation establishes a microscopic connection between equilibrium magnetic configurations and SW excitations. These findings demonstrate a direct transfer of configurational anisotropy into tunable magnonic functionality, highlighting AASI as a versatile platform for geometry-encoded SW architectures.

DOI: 10.1103/mkhw-ltd2

I. INTRODUCTION

Artificial spin ice (ASI) has emerged as a versatile class of magnetic metamaterials comprising lithographically patterned arrays of interacting single-domain ferromagnetic nanoislands. In these systems, lattice geometry enforces dipolar frustration, giving rise to emergent phenomena such as highly degenerate microstates, effective magnetic charge excitations, and microstate-dependent spin-wave (SW) spectra [1–10]. These properties establish ASI as both a model platform for frustrated magnetism and a promising route toward reconfigurable magnonic media, where programmable resonances and tunable mode hybridization enable adaptive microwave functionalities [11–16]. However, the intrinsically discrete and disconnected nature of ASI confines SW excitations to individual nanoislands or vertex regions, thereby limiting coherent propagation lengths and constraining its applicability for extended magnonic transport and passive device architectures [15].

The corresponding inverse structures, termed antiartificial spin ice (AASI), offer a conceptually distinct materials platform in which a continuous ferromagnetic film is patterned with a spin-ice-derived antidot lattice. In this framework, magnetic anisotropy is imposed through geometric boundary conditions rather than interisland dipolar coupling while preserving the vertex topology of spin ice lattices [17,18]. This combination of geometric constraint and magnetic continuity enables collective SW excitations and gives rise to anisotropic, geometry-defined magnonic band structures capable of supporting flat bands, directional transport, and tunable band gaps [16–19]. Consequently, AASI bridges the gap between frustrated magnetism and functional magnonics, providing a scalable route toward robust magnonic crystals, passive waveguides, and lattice-encoded microwave filters governed primarily by geometry.

Despite these advantages, a systematic understanding of how antidot geometry, lattice heterogeneity, and magnetic field orientation collectively determine both magnetization reversal and SW dynamics in AASI remains limited.

*Contact author: adekunle.o.adeyeye@durham.ac.uk

Published by the American Physical Society under the terms of the Creative Commons Attribution 4.0 International license. Further distribution of this work must maintain attribution to the author(s) and the published article's title, journal citation, and DOI.

In particular, bicomponent AASI lattices—where two antidot sublattices with distinct hole dimensions are embedded within a single continuous film—offer an unexplored pathway for engineering spatially varying anisotropy and transferring equilibrium magnetic textures into tailored dynamic responses.

Recent advances further highlight the fundamental richness of AASI systems. Unlike conventional ASI, where frustration arises from competing local constraints, AASI can exhibit topological charge frustration governed by lattice connectivity. In particular, networks composed of odd-sided polygons inhibit long-range charge ordering and give rise to distinct frustration mechanisms associated with charge crystallization and symmetry breaking in the attractive interaction regime [20]. These findings establish AASI as a broader conceptual framework for designing frustration through geometry and topology.

Related insights have been obtained in bicomponent antidot lattices with circular geometries, where controlled variations in hole size modulate the internal magnetic potential landscape, leading to mode splitting, band structure engineering, and hybridized resonances [21,22]. Extending these concepts to spin-ice-derived antidot architectures introduces additional geometric symmetry, offering new opportunities for encoding functionality directly into lattice design.

AASI provides a unique route for translating geometric frustration into functional magnonic behavior. By patterning a continuous ferromagnetic film with spin-ice-derived antidot lattices, AASI overcomes the intrinsic confinement of SW excitations characteristic of conventional ASI and enables collective magnon propagation across extended distances. The resulting geometry-induced modulation of the internal magnetic field creates a potential landscape for SWs, giving rise to anisotropic dispersion, mode localization, tunable band gaps, and field-dependent mode hybridization, which have been utilized in multifunctional microwave and logic applications [16]. These properties establish AASI as an attractive platform for reconfigurable magnonic crystals, passive SW waveguides [23], tunable microwave filters [24], and frequency-selective signal-processing devices [18]. Furthermore, the ability to encode functionality through lattice geometry, combined with the rich dynamical response arising from frustration, positions AASI as a promising candidate for future wave-based computing and neuromorphic magnonic systems.

In this work, the static and dynamic magnetic properties of homogeneous and bicomponent Permalloy AASI lattices are systematically investigated using magneto-optical Kerr effect (MOKE) magnetometry, Brillouin light scattering (BLS) spectroscopy, and micromagnetic simulations. The results establish how geometric design and magnetic field orientation govern magnetization reversal pathways and imprint configurational anisotropy onto the SW spectrum. This direct correspondence between equilibrium magnetization states and magnonic excitations defines a framework for geometry-encoded magnonic functionality in continuous artificial frustrated systems.

II. RESULTS AND DISCUSSION

A. Fabrication of antiartificial spin ice lattices

Three distinct AASI lattices, arranged on a square and rectangular geometry, were fabricated using deep-ultraviolet (DUV) lithography with a 193-nm exposure wavelength on a 5×5 mm^2 Si substrate. The first structure, denoted AASI-S, consists of stadium-shaped antidots with dimensions of 75×210 nm and an edge-to-edge spacing of 160 nm. The second structure, referred to as AASI-L, comprises larger antidots measuring 120×370 nm, with an increased edge-to-edge separation of 190 nm. The third structure, termed AASI-Bi, integrates both antidot sizes within a single lattice, combining 75×210 nm and 120×370 nm holes with anisotropic edge-to-edge spacings of 160 and 190 nm along the x and y directions, respectively. Schematics of the three AASI lattices are shown in Figs. 1(a)–1(c). Details of the adapted fabrication procedure have been reported elsewhere [25]. Following pattern definition, the magnetic AASI structures were realized by depositing a 20-nm thick $Ni_{81}Fe_{19}$ (Permalloy) layer via dc magnetron sputtering from a single target. The base pressure of the sputtering chamber was approximately 1.6×10^{-7} Torr, with a working pressure of 1.3×10^{-3} Torr and a deposition rate of 0.25 Å s^{-1}. A 2-nm Ru capping layer was subsequently deposited at a rate of 0.22 Å s^{-1} to prevent oxidation. Lift-off was performed using ultrasonic agitation in OK73 resist thinner, followed by rinsing in deionized water. The fidelity of the pattern transfer and successful lift-off were confirmed by scanning electron microscopy (SEM), which exhibits high-quality periodic fabrication with well-defined hole shapes and sizes. Representative SEM images of the fabricated AASI-S, AASI-L, and AASI-Bi lattices are shown in Figs. 1(d)–1(f). The dashed areas indicate the unit cell of the AASI lattices. Schematics of the film structure, together with the sample's geometric configuration and coordinate system, are shown in Figs. 1(g)–1(h), respectively. Unit cell dimensions are 370×370 nm for AASI-S, 560×560 nm for AASI-L, and 530×400 nm for AASI-Bi.

The collective magnetization reversal behavior of the AASI lattices was investigated using custom-built longitudinal MOKE magnetometry. An in-plane magnetic field was applied and swept over a range of ± 560 Oe. The relative angle, ϕ, between the applied magnetic field and the AASI unit cell was controlled by rotating the sample in 1° increments over the angular range $0° \leq \phi \leq 180°$ [see Fig. 1(h)]. As all AASI arrays were patterned on the same substrate, identical field orientations were applied to all structures during measurements. SW dynamics were

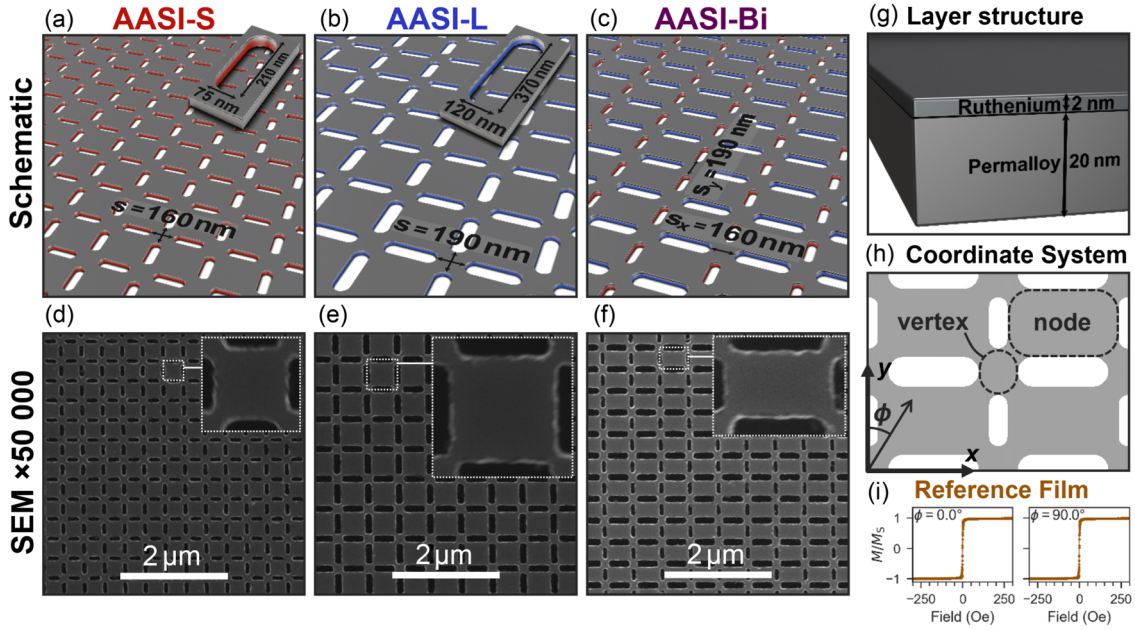


FIG. 1. (a)–(c) Schematic representations of the three AASI geometries: homogeneous lattices with small antidots [AASI-S, (a)], large antidots [AASI-L, (b)], and a bicomponent lattice containing two antidot sizes [AASI-Bi, (c)]. The antidot dimensions and edge-to-edge spacings are indicated in each panel. (d)–(f) Corresponding SEM images of the fabricated lattices, acquired at 50 000× magnification. Insets show enlarged views of the unit cells. (g) Schematic of the film stack consisting of a 20-nm Permalloy layer capped with 2-nm Ru. (h) Definition of the coordinate system used throughout the manuscript, indicating the in-plane field angle ϕ, the lattice node, and the vertex region. (i) Normalized hysteresis loops measured along the two principal in-plane directions ($\phi = 0°$ and $\phi = 90°$) for the unpatterned reference Permalloy film, demonstrating negligible intrinsic in-plane magnetic anisotropy.

characterized using BLS spectroscopy in a backscattering configuration [26], employing a Sandercock-type (3 + 3)-pass tandem Fabry–Perot interferometer [27]. The incident laser beam was fixed at an angle of 10° with respect to the sample normal. In-plane magnetic fields were applied along two distinct lattice orientations, corresponding to $\phi = 0°$ and $\phi = 30°$, and swept from −500 to +500 Oe in steps of 50 Oe to probe the angular dependence of the SW spectra. Micromagnetic simulations were carried out using the MuMax3 simulation package [28]. Standard material parameters for Permalloy were employed: saturation magnetization $M_s = 8.0 \times 10^5$ A m^{-1}, exchange stiffness $A = 1.3 \times 10^{-11}$ J m^{-1}, Gilbert damping parameter $\alpha = 0.008$, and zero magnetocrystalline anisotropy. The geometric dimensions used in the simulations were extracted directly from SEM images of the fabricated structures. The simulation volume comprised a single unit cell of the AASI lattice, discretized into cubic cells of $2.5 \times 2.5 \times 2.5$ nm. Dynamic simulations were performed using a ring-down method, in which a broadband sinc-function magnetic field pulse was applied to uniformly excite SW modes from equilibrium states obtained along the simulated hysteresis loops [29].

B. Static magnetic properties

Figure 1(i) shows the normalized (M/M_s) hysteresis loops of the continuous (unpatterned) Permalloy film measured along two orthogonal in-plane directions ($\phi = 0°$ and $\phi = 90°$). The loops exhibit a nearly square shape with very low coercivity and negligible variation between field orientations, confirming the absence of any significant intrinsic in-plane magnetic anisotropy. This isotropic behavior establishes the continuous film as a suitable reference system for isolating the anisotropic effects introduced by antidot patterning.

Figures 2(a), 2(c), and 2(e) present the angular evolution of the magnetization reversal behavior in the AASI lattices. Pronounced differences are observed among the three geometries, highlighting the dominant role of lattice design in defining the magnetic response. In all patterned systems, the introduction of the antidot lattice leads to a substantial increase in coercivity relative to the continuous film. This enhancement is consistent with increased domain-wall (DW) pinning at the antidot boundaries, where the hole edges act as effective energy barriers to DW propagation. Such behavior is well documented in antidot systems and is typically attributed to the interaction between moving DWs and geometrically defined pinning sites [30,31].

Overall, these results demonstrate that the incorporation of spin-ice-derived antidot geometries not only induces magnetic anisotropy but also fundamentally modifies magnetization reversal pathways through geometry-controlled pinning mechanisms.

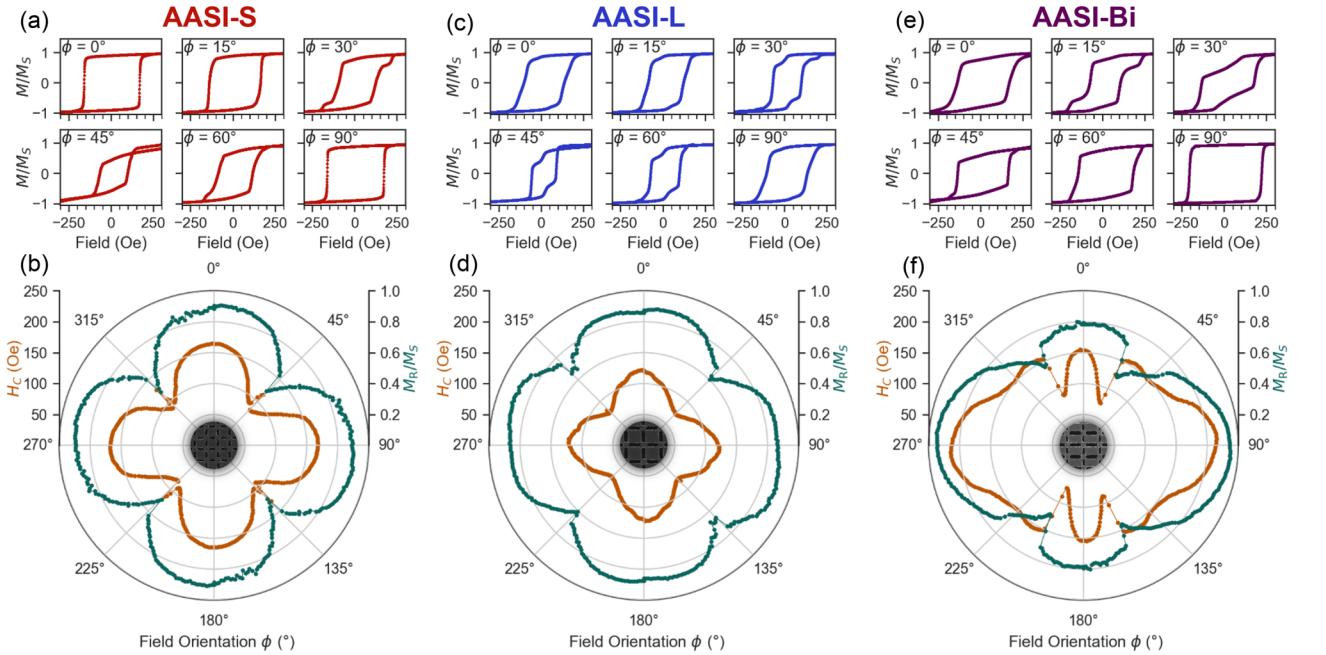


FIG. 2. Angular dependence of the magnetization reversal behavior in the AASI lattices. (a), (c), and (e) Representative normalized hysteresis loops measured at selected in-plane magnetic field orientations ($\phi = 0°, 15°, 30°, 45°, 60°$, and 90°) for the AASI-S, AASI-L, and AASI-Bi lattices, respectively. (b), (d), and (f) Polar plots of the coercive field (H_c) (orange, left axis) and normalized remanent magnetization (M_R/M_s) (green, right axis), as a function of the in-plane field angle for the AASI-S, AASI-L, and AASI-Bi lattices, respectively.

For the homogeneous AASI lattices (AASI-S and AASI-L), the hysteresis loops display a strong dependence on the orientation of the applied magnetic field. In particular, the coercive field (H_c) and loop squareness exhibit pronounced angular variations. Measurements along $\phi = 0°$ and $\phi = 90°$ yield nearly identical, square-shaped loops, reflecting the equivalence of these directions imposed by the fourfold symmetry of the square lattice and identifying them as magnetically easy axes. As the field is rotated toward intermediate orientations (30°–60°), the loops progressively lose squareness and, in some cases, develop multistep switching features, indicative of competing reversal pathways and the emergence of nonuniform magnetization states. A quantitative analysis for the AASI-S lattice is presented in Fig. 2(b), where H_c and the remanent magnetization (M_R) are plotted as a function of ϕ. Both parameters exhibit clear angular anisotropy, with coincident minima at $\phi = \pm 45°$. This behavior highlights the strong configurational anisotropy imposed by the antidot geometry. Specifically, H_c decreases from approximately equal to 165 Oe at $\phi = 0°$ to approximately equal to 82 Oe at $\phi = 45°$, before increasing again toward $\phi = 90°$. A similar trend is observed for M_R, which decreases from approximately equal to 0.90 to 0.51 between 0° and 45°, followed by a recovery at larger angles.

The angular dependence of H_c and M_R for the AASI-L lattice is summarized in Fig. 2(d). While the overall symmetry and angular trends closely resemble those observed for AASI-S, a systematic reduction in the absolute coercive field is evident across all field orientations. For instance, H_c decreases from approximately equal to 120 Oe at $\phi = 0°$ to approximately equal to 72 Oe at $\phi = 45°$, accompanied by a reduction in M_R from approximately equal to 0.88 to 0.60 over the same angular range. This behavior indicates that the larger antidots act as less effective pinning centers compared with the smaller features in AASI-S, thereby facilitating earlier DW nucleation and propagation. These observations underscore the critical role of antidot dimensions in defining the magnetization reversal processes and highlight the sensitivity of static magnetic properties to lattice geometry in AASI systems.

The remanent magnetization in AASI-L preserves the fourfold symmetry imposed by the square lattice, with pronounced minima occurring along the diagonal directions ($\phi = 45°, 135°$, and equivalent orientations). However, the modulation depth of M_R is reduced compared with AASI-S, indicating a weaker angular variation of the magnetic configuration. Furthermore, AASI-L exhibits more pronounced steplike switching features, particularly at intermediate field orientations [see Fig. 2(c) for $\phi = 30°, 45°$, and 60°], suggesting a multistage reversal process involving distinct magnetization subconfigurations.

Overall, AASI-L is characterized by higher and more uniform remanence, reduced angular modulation, and less pronounced minima. This behavior is attributed to the

larger unit-cell dimensions, which reduce local demagnetizing effects and promote more continuous magnetic pathways. In particular, the minima in H_c and M_R observed at $\phi = 45°$ are associated with preferential reversal along continuous Permalloy channels aligned with these directions, effectively lowering the energy barrier for magnetization switching.

More generally, the well-defined angular dependence in both homogeneous lattices reflects a geometry-driven anisotropy landscape. The reduction in M_R and the distortion of the hysteresis loops at intermediate angles indicate the presence of competing reversal pathways and metastable magnetic states, arising from geometry-induced energy barriers rather than strong disorder or highly degenerate configurations.

In contrast to the homogeneous systems, the bicomponent AASI-Bi lattice exhibits a markedly enhanced angular anisotropy and a qualitatively different magnetization reversal behavior. The hysteresis loops show a significantly stronger dependence on the field orientation, arising from the reduced symmetry of the lattice. This symmetry breaking originates from the coexistence of two antidot sublattices with distinct hole sizes and anisotropic edge-to-edge spacings, resulting in a more complex magnetic energy landscape. As shown in Fig. 2(e), the evolution of the hysteresis loops with ϕ reveals substantial variations in both loop shape and switching characteristics compared with the homogeneous lattices. At comparable field orientations, the loops display distinct features and multistep switching. In particular, a clear two-stage reversal process is observed around $\phi \approx 15°$, indicating the presence of sequential switching events associated with different regions of the heterogeneous lattice.

The corresponding angular dependence of H_c and M_R is presented in Fig. 2(f). In contrast to the fourfold symmetric behavior of the homogeneous lattices, the AASI-Bi structure exhibits a shifted anisotropy landscape. At $\phi = 0°$, the remanent magnetization is lower than in AASI-S and AASI-L, whereas at $\phi = 90°$, it exceeds that of both systems. Quantitatively, H_c increases from approximately equal to 155 Oe at $\phi = 0°$ to approximately equal to 215 Oe at $\phi = 90°$, while M_R rises from approximately equal to 0.78 to 0.95 over the same angular range. Notably, the coercivity minimum is shifted from $\phi \approx 45°$ in the homogeneous lattices to approximately equal to 23° in the bicomponent structure. This shift is attributed to the emergence of preferential reversal pathways along continuous Permalloy segments aligned with specific crystallographic directions defined by the asymmetric rectangular unit cell of the lattice. These effective magnetic channels exhibit reduced shape anisotropy and facilitate DW motion, thereby lowering the energy barriers for magnetization reversal. Because of the modified lattice symmetry, the orientation of these pathways is rotated relative to the homogeneous case, resulting in the observed displacement of the anisotropy extrema. Overall, the AASI-Bi lattice demonstrates that lattice heterogeneity provides an additional degree of freedom for engineering the magnetic anisotropy landscape and reversal pathways. These results highlight the potential of bicomponent AASI architectures for tailoring static magnetic properties beyond the limits of homogeneous designs.

In comparison with conventional antidot arrays based on circular holes, where shape-induced anisotropy is typically weak, the AASI geometry enables significantly enhanced control of magnetic anisotropy through deliberate lattice design. Previous studies on circular antidot lattices have shown that magnetic anisotropy is primarily governed by lattice symmetry and spatial arrangement rather than by the individual hole geometry [31]. In the present case, the overall lattice symmetry is largely preserved across the homogeneous AASI structures, allowing a more direct assessment of the role of antidot size and shape. The observed variations in magnetization reversal behavior between AASI-S and AASI-L, therefore, originate predominantly from differences in antidot dimensions rather than from changes in lattice symmetry. This demonstrates that the stadium-shaped geometry introduces a strong form of configurational anisotropy, which is absent in simpler circular systems. As a result, the balance between DW pinning, dipolar interactions, and magnetic frustration is effectively tuned by modifying the antidot geometry. These findings highlight that both the size and shape of the antidots play a decisive role in controlling the magnetization reversal process. More broadly, they establish geometry as a primary design parameter for tailoring static magnetic properties in AASI systems, enabling a level of anisotropy engineering that extends beyond that achievable in conventional antidot lattices.

To further elucidate the static magnetic behavior of the three AASI lattices and rationalize the experimentally observed hysteresis characteristics, micromagnetic simulations were performed using the MuMax3 simulation package [28]. Figure 3 shows the simulated hysteresis loops for AASI-S (a), AASI-L (b), and AASI-Bi (c) with the magnetic field applied along $\phi = 0°$, together with representative magnetization configurations extracted along the ascending branch of the M-H curves, starting from negative saturation ($H = -400$ Oe). The simulations reproduce the key experimental trends, establishing a direct correspondence between the loop shapes and the geometry-driven reversal mechanisms.

For the homogeneous lattices, both AASI-S and AASI-L exhibit predominantly single-step switching behavior, consistent with the experimental results. The simulated coercive field is systematically larger for AASI-S, confirming stronger DW pinning associated with the smaller antidots. At large negative fields ($H \approx -400$ Oe), AASI-S approaches a quasi-uniform magnetization state, with spins aligned along the field direction. In this regime,

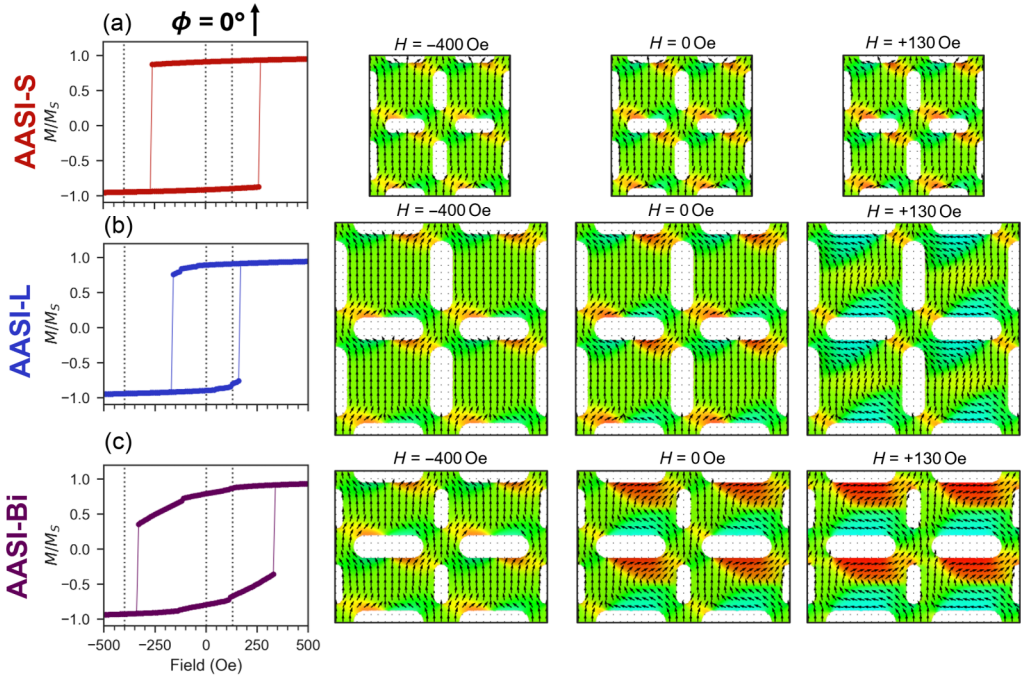


FIG. 3. Micromagnetic simulation results for magnetization reversal in antiartificial spin ice at $\phi = 0°$. (a)–(c) Simulated hysteresis loops (M/M_s vs H) of the AASI-S, AASI-L, and AASI-Bi lattices obtained from MuMax3 simulations with the applied in-plane magnetic field oriented at $\phi = 0°$. Magnetization snapshots corresponding to the marked positions on each hysteresis loop are shown to the right. In the snapshots, arrows represent the local magnetization direction, and superimposed streamlines trace the magnetization vector field. The streamline density is included for visualization purposes only and does not represent magnetic field magnitude or strength.

the continuous regions of the film (nodes) and the narrower interconnections (vertices), defined in Fig. 1(h), remain uniformly magnetized, while DWs form along the connecting pathways and curve around the antidots to minimize magnetostatic energy. Upon reducing the field toward zero, these DWs gradually expand and redistribute, indicating that reversal is dominated by DW motion rather than coherent rotation.

In AASI-L, the magnetization remains largely uniform at high negative fields, but noticeable distortions emerge near the antidot boundaries, reflecting an increased competition between exchange and demagnetizing energies. At zero field, these distortions intensify, and at $H = +130$ Oe, the system transitions to a nonuniform S-state within the node regions. This configuration is characterized by elongated horizontal channels and pronounced transverse magnetization components near the long edges of the antidots, indicative of intermediate states during reversal. Consequently, the hysteresis loop evolves more gradually than in AASI-S, consistent with a multistage reversal process involving the nucleation and propagation of nonuniform magnetization textures.

The AASI-Bi lattice exhibits the most complex reversal behavior. The simulated loop [Fig. 3(c)] displays a slanted profile followed by a dominant switching event, in agreement with the experiment. Even at $H = -400$ Oe, the magnetization already shows significant bending and spatial nonuniformity near antidot boundaries, highlighting the strongly anisotropic energy landscape imposed by the heterogeneous geometry. At remanence ($H = 0$ Oe), extensive redistribution of the magnetization is observed, indicating a substantial departure from the saturated state. At $H = +130$ Oe, well-defined horizontal channels dominate the spin structure, accompanied by large regions of transverse alignment and flux-guided configurations. The node regions develop pronounced C-states, reflecting strong magnetostatic interactions and flux-closure effects. Correspondingly, the AASI-Bi hysteresis loop exhibits the least-square shape and the most gradual evolution among all lattices, indicative of multiple metastable states during reversal. These results demonstrate that the bicomponent architecture promotes complex reversal pathways involving domain reorganization, enhanced magnetostatic coupling, and the stabilization of intermediate magnetic configurations before full switching.

Figure 4 presents the simulated hysteresis loops for the AASI-S, AASI-L, and AASI-Bi lattices with the in-plane magnetic field applied at $\phi = 30°$, together with representative magnetization configurations at selected field values along the reversal process. For the homogeneous lattices [AASI-S and AASI-L; Figs. 4(a) and 4(b)], the simulations reveal pronounced multistep switching behavior, with three distinct features evident in the hysteresis loops. At large negative fields ($H \approx -400$ Oe), the

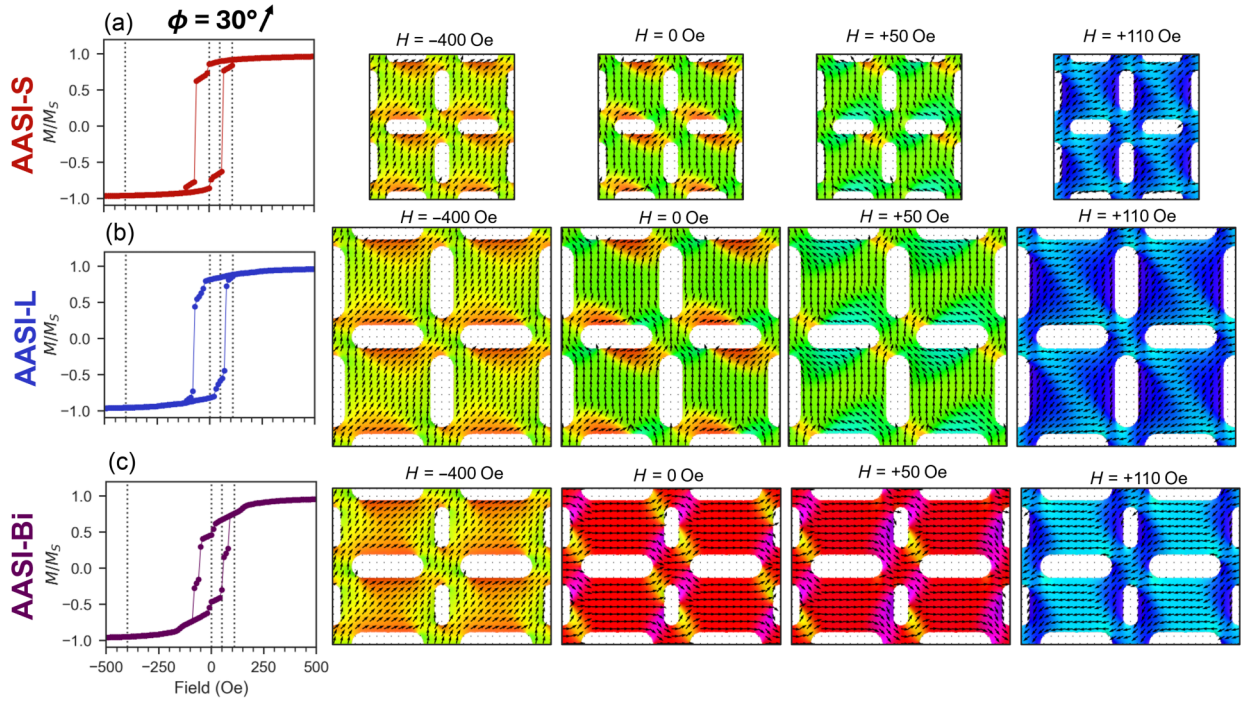


FIG. 4. Micromagnetic simulation of magnetization reversal in antiartificial spin ice at $\phi = 30°$. (a)–(c) Simulated hysteresis loops (M/M_s vs H) of the AASI-S, AASI-L, and AASI-Bi lattices obtained from MuMax3 simulations with the applied in-plane magnetic field oriented at $\phi = 30°$. Magnetization snapshots corresponding to the marked positions on each hysteresis loop are shown to the right of the respective curves. In the snapshots, arrows indicate the local magnetization direction, while overlaid streamlines trace the magnetization vector field. The streamline density is used for visualization purposes only and does not represent magnetic field magnitude or strength.

magnetization within both nodes and vertices is largely aligned with the applied field, while DWs are stabilized along the interconnecting regions and curve around the antidot boundaries to minimize magnetostatic energy. As the field is reduced, the magnetization progressively reorients toward the y direction, reflecting the influence of geometry-imposed shape anisotropy. At intermediate fields, the reduced Zeeman contribution favors alignment along the antidot edges, driving a gradual rotation of the magnetization within the nodes. This process provides a microscopic origin for the experimentally observed reduction in remanent magnetization with increasing field angle. The initial switching feature corresponds to DW depinning and propagation along the horizontal antidot channels; however, this contribution is less pronounced in AASI-S and is not clearly resolved experimentally. The dominant switching event is associated with the formation of a configuration in which the magnetization aligns preferentially along a lattice direction ($\phi \approx 60°$), rather than along the external field. This state minimizes magnetostatic energy through the expansion and alignment of connecting DWs. In AASI-L, the larger antidots give rise to broader and smoother switching features, consistent with the experimentally observed gradual loop evolution.

For the bicomponent lattice [Fig. 4(c)], a qualitatively different response is observed. A distinct change in the magnetization gradient appears at $H \approx -150$ Oe, corresponding to a reorientation of the magnetization toward the horizontal edges of the larger antidots. While this configuration increases the Zeeman energy, it significantly reduces demagnetizing energy due to the size asymmetry between the two antidot sublattices, rendering it energetically favorable. At remanence, the magnetization is predominantly aligned along the horizontal large-antidot channels, although this state is less pronounced experimentally, likely due to higher depinning fields. At $H \approx +130$ Oe, the spin texture differentiates into two distinct regions: areas near the vertical edges of the larger antidots exhibit nearly complete reversal, while node regions remain aligned along the horizontal direction. These horizontal regions form effective, continuous channels acting as preferential pathways for magnetization, analogous to waveguidelike features within the lattice.

Overall, the simulations identify two distinct reversal regimes depending on field orientation. At lower angles, reversal proceeds via the formation of bisecting DWs that reduce magnetostatic energy with minimal Zeeman variation. At higher angles, DW rotation and depinning dominate the process, leading to multistage switching and complex hysteresis behavior. These results provide a consistent microscopic framework for interpreting the angular-dependent magnetic response of both homogeneous and bicomponent AASI lattices.

The quantitative discrepancy between the experimental and simulated coercive fields can be attributed to the inherent challenges associated with predicting coercivity quantitatively using micromagnetic simulations. In contrast to quantities such as the loop saturation magnetization and remanence, the coercive field is not determined solely by the intrinsic magnetic parameters of the material. However, quantitative prediction of the coercive field is known to be particularly challenging in micromagnetic simulations. In contrast to quantities such as the saturation magnetization or the magnetocrystalline anisotropy, the coercive field is not determined solely by the intrinsic magnetic parameters of the material. This issue is closely related to the well-known Brown coercivity paradox, namely, the long-standing observation that the experimentally measured coercive fields of real magnetic materials are often substantially lower than the values expected for ideal defect-free systems based only on their intrinsic magnetic parameters [32]. In real materials, reversal generally starts at local weak points or defects and subsequently proceeds through DW propagation or other nonuniform reversal processes. Consequently, even relatively small local imperfections can strongly reduce the experimentally observed coercive field [33].In AASI, magnetization reversal is governed by DW nucleation and depinning processes that are highly sensitive to edge roughness, defects, and local pinning sites. While the simulations employ periodic boundary conditions and an idealized defect-free unit cell, the experimental structures contain unavoidable fabrication-induced distributions of geometrical parameters that influence the switching field. In addition, the MOKE measurements represent an average over a large number of unit cells with a distribution of local coercivities, whereas the simulations describe a single idealized cell. Therefore, some quantitative difference in H_c is expected, even though the simulations successfully reproduce the experimentally observed reversal pathways and magnetic configurations.

C. Dynamic magnetic properties

To complement the static magnetization analysis and elucidate the impact of reversal mechanisms on the dynamic response, the angular dependence of SW excitations in the AASI lattices was investigated using BLS spectroscopy.

Figures 5(a) and 5(b) present the room-temperature BLS spectra recorded under a saturating magnetic field ($H = -500$ Oe) applied along $\phi = 0°$ and $\phi = 30°$, respectively, for all three AASI lattices. In all cases, symmetric Stokes and anti-Stokes peaks are observed, exhibiting similar frequencies but asymmetric intensities. For $\phi = 0°$ [Fig. 5(a)], the AASI-S lattice exhibits three principal resonances. A broad low-frequency mode appears around 4–5 GHz (mode 1), while the dominant resonance (mode 2) is centered near 8.4 GHz. A weaker, high-frequency feature

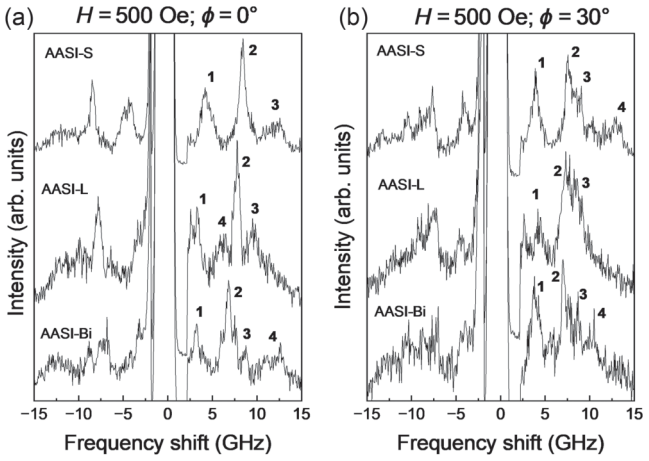


FIG. 5. Sequences of room-temperature BLS spectra for the three AASI lattices measured under a saturating magnetic field of $H = -500$ Oe applied at (a) $\phi = 0°$ and (b) $\phi = 30°$ directions. The spectra are vertically offset for clarity. The labeled peaks (1–4) identify the main SW modes observed in each lattice.

(mode 3) is observed around 12–13 GHz. In the AASI-L lattice, the spectral response becomes richer, with the emergence of an additional resonance (mode 4) near 6 GHz. The dominant mode shifts to lower frequency (approximately equal to 7.8 GHz), while the higher-frequency mode becomes sharper and more defined around 9.7 GHz. The AASI-Bi lattice exhibits the most complex spectrum, characterized by four well-resolved modes. The dominant peak further shifts to approximately equal to 6.7 GHz and is accompanied by additional satellite features, with modes distributed near 3, 9, and a strong high-frequency resonance around 12–13 GHz.

At $\phi = 30°$ [Fig. 5(b)], all lattices exhibit an overall increase in spectral complexity, while all observed peaks undergo a downward frequency shift. For AASI-S, four modes are clearly resolved, with the dominant resonance appearing near 7.7 GHz and additional features at approximately equal to 5, 8.7, and 13–14 GHz. In AASI-L, the modes become more closely spaced and broadened, with enhanced intensity of higher-frequency peaks, indicating increased contributions from localized or higher-order excitations. The AASI-Bi lattice again displays the richest spectrum, with four distinct modes distributed around approximately equal to 4, 7, 9, and 12–13 GHz. In comparison to the homogeneous lattices, the dominant mode becomes broader and less intense, while higher-order modes gain spectral weight. This behavior reflects the increased magnetic heterogeneity introduced by the bicomponent geometry, which leads to a progressive enrichment of the SW spectrum, reflected in the appearance of additional modes, frequency shifts, and enhanced mode splitting.

Figure 6(a) presents the field-dependent BLS spectra of the AASI-S lattice for $\phi = 0°$. Three principal modes are

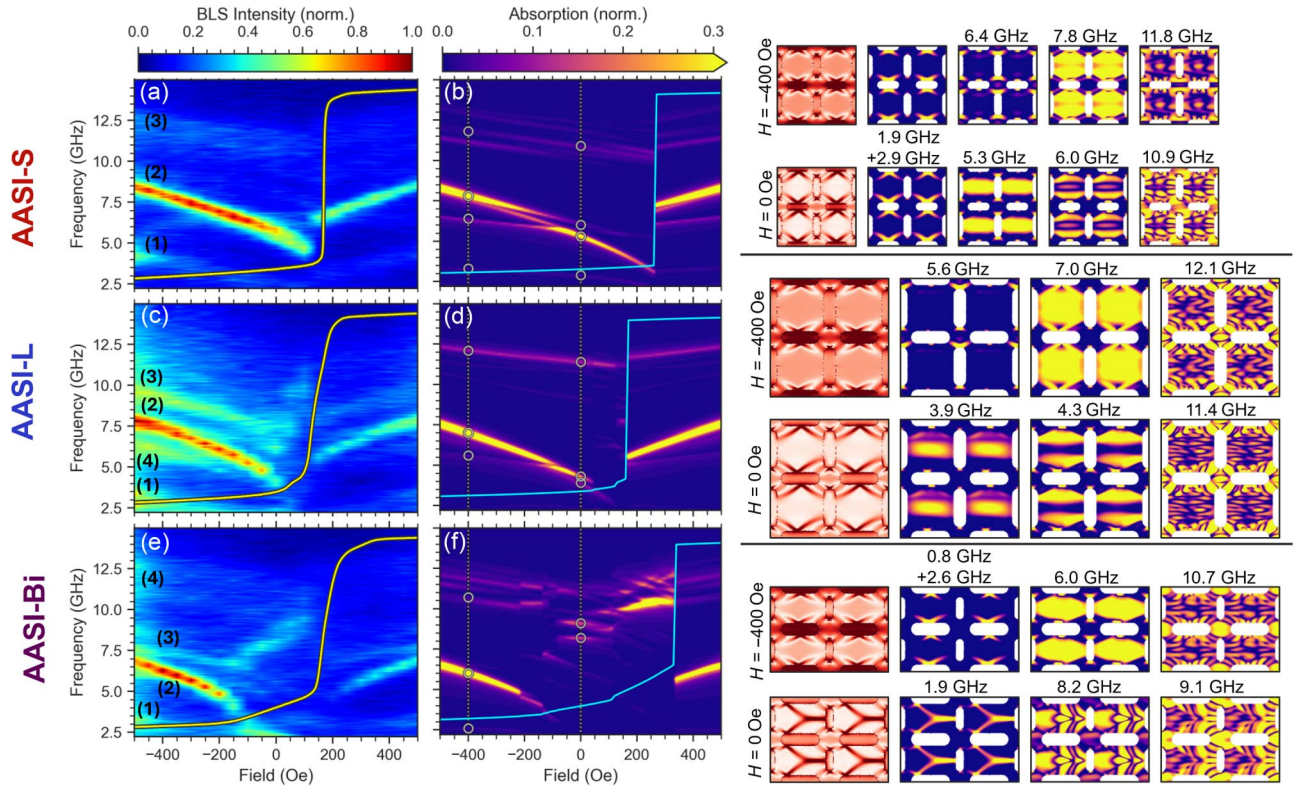


FIG. 6. Spin-wave spectra of antiartificial spin ice lattices measured at $\phi = 0°$. (a), (c), and (e) Two-dimensional BLS spectra of the AASI-S, AASI-L, and AASI-Bi lattices, respectively, measured with the applied in-plane magnetic field oriented at $\phi = 0°$. All BLS measurements were performed with a fixed light incidence angle of 10°. (b), (d), and (f) Corresponding two-dimensional absorption spectra obtained from micromagnetic simulations for the AASI-S, AASI-L, and AASI-Bi lattices at $\phi = 0°$. The ascending branch of the measured MOKE loop is also plotted for comparison in panels (a), (c), and (e). Representative effective-field distributions and spin-wave mode profiles at selected applied fields are shown. The selected fields are indicated by vertical lines in the simulated spectra, with the corresponding mode profiles marked by open circles.

resolved, with mode (2) dominating the spectral response. Its frequency decreases monotonically, as the field approaches the reversal region (approximately equal to +150 Oe) and increases again afterward, forming a characteristic V-shaped dependence associated with the fundamental SW mode. In contrast, the low-frequency mode (1) (approximately equal to 2.5–4 GHz) and the high-frequency mode (3) (approximately equal to 10–12 GHz) are broader and weaker, exhibiting an approximately linear field dependence and only minor discontinuities at switching. Micromagnetic simulations [Fig. 6(b)] reproduce the overall spectral evolution and enable mode assignment. Mode (2) is identified as the quasi-uniform (Kittel-like) mode localized within the node regions, accounting for its high intensity. The low-frequency response corresponds to edge-localized modes, split into two branches (approximately equal to 2.2 and 3.3 GHz) due to spatial asymmetry of the internal field; these modes are confined near antidot boundaries and exhibit characteristic "sicklelike" profiles, explaining their weak spectral intensity. A weaker mode near approximately equal to 6 GHz is attributed to a vertex-localized excitation that hybridizes with the fundamental mode at higher fields. The high-frequency mode (approximately equal to 11–12 GHz) originates from strongly localized vertex oscillations with a nodal structure perpendicular to the applied field. Additional modes predicted by simulations are not experimentally resolved, likely due to their low intensity.

Overall, the combined experimental and numerical analysis establishes a clear correspondence between mode localization, internal field distribution, and the observed SW spectra.

The BLS spectra of the AASI-L lattice for $\phi = 0°$ [Fig. 6(c)] reveal a richer modal structure compared with AASI-S, with four distinct resonances. While the overall field dependence remains qualitatively similar, notable differences emerge in both frequency evolution and mode intensity. The lowest-frequency mode (1) is only resolved at high fields, where its frequency exceeds approximately equal to 2.5 GHz, falling below the experimental detection limit at lower fields. In contrast, the dominant mode (2), located near approximately equal to 7.5 GHz at large negative fields, exhibits a pronounced frequency softening as the system approaches reversal, reaching

approximately equal to 4 GHz near the switching field. This enhanced softening relative to AASI-S indicates a stronger reduction of the effective internal field, arising from geometry-driven redistribution of magnetostatic interactions.

The higher-frequency mode (3) remains observable throughout the field sweep but displays a distinct spectral signature. It appears sharper and more intense, with only weak field dependence, remaining within approximately equal to 8–10 GHz. Near the reversal region (0 to +100 Oe), the spectra become diffuse and additional quasi-field-independent modes emerge, reflecting the formation of nonuniform magnetic configurations. At higher positive fields, well-defined modes reappear, recovering the linear field dependence characteristic of a uniformly magnetized state.

Micromagnetic simulations [Fig. 6(d)] reproduce the main spectral features, including the additional mode (4), and identify a fundamental mode (approximately equal to 7 GHz) together with edge-localized excitations (approximately equal to 0.9 and 2.3 GHz). Experimentally observed modes near approximately equal to 6.1 and 9.2 GHz are only partially captured, likely corresponding to vertex-localized excitations (approximately equal to 5.6 and 10.9 GHz) in the simulations. A predicted splitting of the fundamental mode at low fields due to vertex localization is not resolved experimentally, likely due to limited frequency separation.

Figure 6(e) presents the field-dependent BLS spectra of the AASI-Bi lattice for $\phi = 0°$. At high negative fields ($H \approx -400$ Oe), three distinct modes are observed, all exhibiting a monotonic frequency decrease as the field approaches reversal. The dominant mode (2) shows pronounced frequency softening compared with the homogeneous lattices, shifting from approximately equal to 6–7 GHz at large negative fields to approximately equal to 4 GHz near the switching region, where it becomes indistinguishable. This enhanced softening reflects a stronger reduction of the effective internal field induced by the increased geometric complexity.

The low-frequency mode (1), detected around approximately equal to 3.2 GHz at $H = -400$ Oe, is associated with edge-localized excitations. Simulations [Fig. 6(f)] indicate that these modes track the spatial profile of DWs at remanence, highlighting their sensitivity to nonuniform magnetization textures. In contrast, the higher-frequency mode (3) exhibits a distinct behavior: instead of softening, it splits into a doublet that dominates the spectrum in the vicinity of reversal (−100 to +100 Oe). This splitting, together with the continuous evolution of the mode frequencies, indicates the presence of multiple metastable magnetic states and strongly nonuniform internal fields that promote interaction and hybridization between SW eigenmodes.

Micromagnetic simulations reproduce the principal experimental features, including the strong softening and eventual suppression of the fundamental mode. Additional weak, nearly dispersionless modes observed near approximately equal to 8–9 GHz are also captured, further confirming the emergence of multiple localized excitations. Analysis of the simulated mode profiles shows that the dominant mode remains primarily localized within the node regions across all lattices. The progressive reduction in its frequency from AASI-S to AASI-Bi is attributed to enhanced demagnetizing effects and reduced effective field associated with increasing geometric complexity.

Overall, the bicomponent lattice supports a larger number of dynamically active regions, leading to mode splitting, frequency renormalization, and enhanced localization. The very good agreement between experiment and simulation demonstrates that geometrical engineering provides an effective route for tailoring SW spectra, establishing AASI as a versatile platform for reconfigurable magnonic functionalities.

Figure 7(a) presents the two-dimensional BLS spectra of the AASI-S lattice for an in-plane magnetic field applied at $\phi = 30°$. Compared with the $\phi = 0°$ configuration, a larger number of modes is resolved, reflecting enhanced magnetic nonuniformity at this orientation. At high negative fields ($H \approx -400$ Oe), four well-defined modes are observed alongside weaker high-frequency features. As the field approaches the reversal regime, all dominant modes soften, and within the field interval approximately equal to 50–150 Oe, the fundamental mode exhibits a pronounced frequency flattening, coinciding with the plateau region observed in the M-H loop. Micromagnetic simulations [Fig. 7(b)] reproduce the main experimental features, although additional modes predicted numerically are not resolved experimentally, probably due to their reduced intensity associated with the large number of nodal lines in their spatial profiles. At $H \approx -400$ Oe, the fundamental and edge modes appear experimentally at approximately equal to 7.5 and 4.0 GHz, in good agreement with simulated values of approximately equal to 7.2 and 4.6 GHz. The fundamental mode splits into closely spaced branches localized within the node regions, while higher-frequency simulated modes correspond to strongly localized excitations. Significantly, the simulations capture the experimentally observed mode flattening near approximately equal to 5.5 GHz, linking this feature to the evolution of the equilibrium magnetization during reversal.

The AASI-L lattice at $\phi = 30°$ [Fig. 7(c)] exhibits a richer dynamic response, with four prominent modes at large negative fields. As the field is increased, all modes soften monotonically, with the lowest-frequency modes (1 and 2) showing pronounced frequency reduction

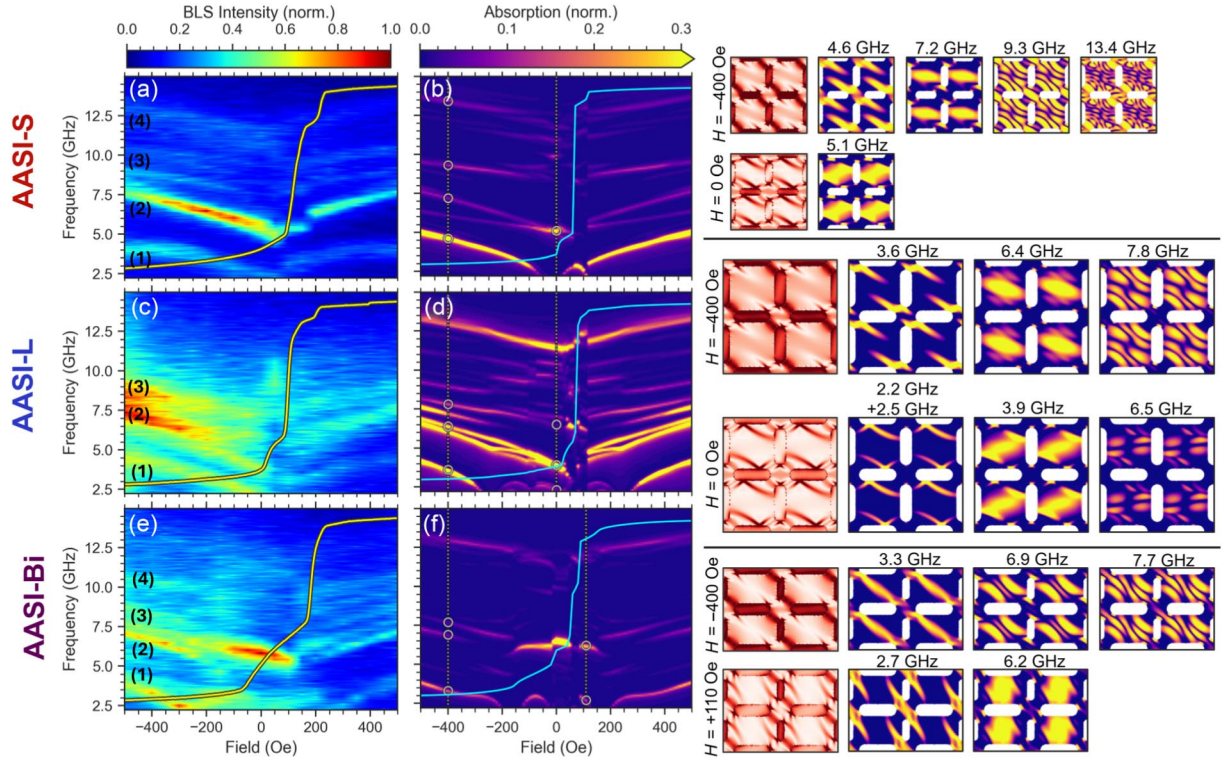


FIG. 7. Spin-wave spectra of antiartificial spin ice lattices measured at $\phi = 30°$. (a), (c), and (e) Two-dimensional BLS spectra of the AASI-S, AASI-L, and AASI-Bi lattices, respectively, measured with the applied in-plane magnetic field oriented at $\phi = 30°$. All BLS measurements were performed with a fixed light incidence angle of 10°. (b), (d), and (f) Corresponding two-dimensional absorption spectra obtained from micromagnetic simulations for the AASI-S, AASI-L, and AASI-Bi lattices at $\phi = 30°$. Representative effective field distributions and spin-wave mode profiles at selected applied fields are shown. The selected fields are indicated by vertical lines in the simulated spectra, with the associated mode profiles marked by open circles.

(approximately equal to 6.0–2.5 GHz) toward the reversal region. Higher-frequency modes (3 and 4) are broader and more intense, indicating a stronger dynamic contribution and greater spatial extent. Near reversal, the spectrum becomes diffuse and is dominated by quasi-field-independent modes in the approximately equal to 7.5–10 GHz range, consistent with highly nonuniform magnetic states. Upon further increasing the field, the modes recover their intensity and linear field dependence, displaying a nearly symmetric evolution across the reversal region. Micromagnetic simulations [Fig. 7(d)] reproduce the multitude of modes observed in BLS. At $H \approx -400$ Oe, the fundamental and edge modes appear at approximately equal to 7.0 and 4.2 GHz, in good agreement with simulated values of approximately equal to 7.0 and 3.7 GHz. The simulated fundamental mode is composed of two individual modes localized in the node that decrease in frequency monotonically until the switching. The edge mode and higher-frequency modes, however, terminate at a lower field.

Figure 7(e) presents the field-dependent BLS spectra of the AASI-Bi lattice for an in-plane magnetic field applied at $\phi = 30°$. At large negative fields ($H \approx -400$ Oe), four main modes are resolved, comprising a low-frequency edge mode near approximately equal to 3.5 GHz and two higher-frequency modes at approximately equal to 7.1 and 7.8 GHz, together with weaker features above 10 GHz. A key distinguishing feature relative to the homogeneous lattices is the emergence of a strong resonance around approximately equal to 6.0–6.5 GHz within the field interval −100 to +100 Oe, corresponding to the onset of magnetization reorientation. Micromagnetic simulations [Fig. 7(f)] reproduce these characteristics, identifying the low-frequency mode as an edge-localized excitation with magnon nanochannellike behavior along the boundaries of the larger antidots. The higher-frequency modes deviate from the fundamental response observed in homogeneous lattices, reflecting the modified mode structure introduced by lattice heterogeneity. The prominent mode near approximately equal to 6 GHz is captured in the simulations at approximately equal to 6.2 GHz, while additional calculated modes remain experimentally unresolved due to their low intensity. Notably, the simulated edge-mode profiles reveal a progressive rotation toward the rounded ends of the antidots as the field varies, emphasizing the sensitivity of the dynamic response to DW configurations.

Regarding the quantitative comparison between the BLS measurements and the micromagnetic simulations, we

emphasize that the frequency of the fundamental SW mode provides the most rigorous benchmark for assessing agreement. This mode produces the strongest BLS signal and represents the most spatially extended excitation in the simulated mode profiles, making it the least susceptible to uncertainties associated with localized defects, edge roughness, or finite experimental resolution. Significantly, the simulations reproduce the frequency of this dominant mode well for all samples studied using the same set of magnetic parameters. This level of agreement demonstrates that the simulations correctly describe the underlying effective-field landscape and the principal SW dynamics of the AASI structures. Any remaining discrepancies are associated primarily with weaker, more localized higher-order modes, which are inherently more sensitive to fabrication-induced inhomogeneities and experimental averaging effects that are not captured in the idealized computational model.

Overall, the BLS results at $\phi = 30°$ demonstrate that both antidot size and lattice heterogeneity strongly influence the SW spectra. The excellent agreement between experiment and simulation confirms that changes in equilibrium magnetization—particularly DW formation and rotation—are directly encoded in the dynamic response. This establishes AASI lattices as a versatile platform for geometry-driven tuning of magnonic excitations and reconfigurable SW functionalities.

III. CONCLUSIONS

In summary, we have demonstrated that antiartificial spin ice provides a robust and versatile platform for engineering both static and dynamic magnetic properties through geometric design. By systematically comparing homogeneous and bicomponent Permalloy antiartificial spin ice lattices and combining magneto-optical Kerr effect measurements, Brillouin light scattering spectroscopy, and micromagnetic simulations, we establish how antidot size, lattice heterogeneity, and field orientation collectively govern magnetization reversal pathways and spin-wave excitations in continuous magnetic media. Our results show that geometrically induced anisotropy imposed by the antidot architecture leads to pronounced angular anisotropy in coercivity and remanent magnetization, with bicomponent lattices exhibiting qualitatively distinct reversal behavior and shifted anisotropy extrema relative to homogeneous arrays. These static magnetic characteristics are directly reflected in the spin-wave response, where domain-wall formation, redistribution, and pinning give rise to geometry- and angle-dependent magnon spectra featuring edge- and node-localized modes, mode splitting, and band flattening. Significantly, the close agreement between experimental observations and micromagnetic simulations provides a consistent microscopic picture linking equilibrium magnetization textures to the observed dynamic modes. Taken together, this work highlights how frustration embedded in a connected magnetic medium can be harnessed to transfer geometric control from static magnetization states to dynamic spin-wave functionality. The demonstrated sensitivity of the magnonic response to lattice design and field direction underscores the potential of antiartificial spin ice for geometry-encoded magnonic crystals, angularly tunable filters, and passive spin-wave waveguides, without reliance on complex magnetic state preparation. More broadly, these findings establish antiartificial spin ice as a promising materials platform for exploring frustrated magnonics and for developing scalable, functionally programmable spin-wave-based devices.

ACKNOWLEDGMENTS

The authors thank Dr. Navab Singh for the DUV templates. SEM imaging of the patterned structures was carried out at the GJ Russell Electron Microscope Facility. A. O. A. expresses gratitude for the Royal Society Wolfson Fellowship. This work has used Durham University's NCC cluster. NCC has been purchased through Durham University's strategic investment funds and is installed and maintained by the Department of Computer Science.

DATA AVAILABILITY

There are no publicly available research data or software supporting this manuscript. Requests for further information or data should be sent to the authors.

[1] R. F. Wang *et al.*, Artificial spin ice in a geometrically frustrated lattice of nanoscale ferromagnetic islands, Nature (London) **439**, 303 (2006).

[2] C. Nisoli, R. Moessner, and P. Schiffer, Colloquium: Artificial spin ice: Designing and imaging magnetic frustration, Rev. Mod. Phys. **85**, 1473 (2013).

[3] S. H. Skjærvø, C. H. Marrows, R. L. Stamps, and L. J. Heyderman, Advances in artificial spin ice, Nat. Rev. Phys. **2**, 13 (2020).

[4] C. Castelnovo, R. Moessner, and S. L. Sondhi, Magnetic monopoles in spin ice, Nature (London) **451**, 42 (2008).

[5] L. Berchialla, G. M. Macauley, and L. J. Heyderman, Focus on three-dimensional artificial spin ice, Appl. Phys. Lett. **125**, 220501 (2024).

[6] J. C. Gartside, K. D. Stenning, A. Vanstone, H. H. Holder, D. M. Arroo, T. Dion, F. Caravelli, H. Kurebayashi, and W. R. Branford, Reconfigurable training and reservoir computing in an artificial spin-vortex ice via spin-wave fingerprinting, Nat. Nanotechnol. **17**, 460 (2022).

[7] A. May, M. Saccone, A. van den Berg, J. Askey, M. Hunt, and S. Ladak, Magnetic charge propagation upon a 3D artificial spin-ice, Nat. Commun. **12**, 3217 (2021).

[8] J. Sklenar, Y. Lao, A. Albrecht, J. D. Watts, C. Nisoli, G.-W. Chern, and P. Schiffer, Field-induced phase coexistence in an artificial spin ice, Nat. Phys. **15**, 191 (2019).

[9] H. Arava, N. Leo, D. Schildknecht, J. Cui, J. Vijayakumar, P. M. Derlet, A. Kleibert, and L. J. Heyderman, Engineering relaxation pathways in building blocks of artificial spin ice for computation, Phys. Rev. Appl. **11**, 054086 (2019).

[10] A. Farhan, P. M. Derlet, A. Kleibert, A. Balan, R. V. Chopdekar, M. Wyss, J. Perron, A. Scholl, F. Nolting, and L. J. Heyderman, Direct observation of thermal relaxation in artificial spin ice, Phys. Rev. Lett. **111**, 057204 (2013).

[11] G. Gubbiotti, X. Zhou, Z. Haghshenasfard, M. G. Cottam, and A. O. Adeyeye, Reprogrammable magnonic band structure of layered permalloy/Cu/permalloy nanowires, Phys. Rev. B **97**, 134428 (2018).

[12] B. Flebus *et al.*, The 2024 magnonics roadmap, J. Phys. Condens. Matter **36**, 363501 (2024).

[13] S. Gliga, E. Iacocca, and O. G. Heinonen, Dynamics of reconfigurable artificial spin ice: Toward magnonic functional materials, APL Mater. **8**, 040911 (2020).

[14] J. C. Gartside, A. Vanstone, T. Dion, K. D. Stenning, D. M. Arroo, H. Kurebayashi, and W. R. Branford, Reconfigurable magnonic mode-hybridisation and spectral control in a bicomponent artificial spin ice, Nat. Commun. **12**, 2488 (2021).

[15] S. Lendinez and M. B. Jungfleisch, Magnetization dynamics in artificial spin ice, J. Phys. Condens. Matter **32**, 013001 (2019).

[16] M. Krawczyk and D. Grundler, Review and prospects of magnonic crystals and devices with reprogrammable band structure, J. Phys. Condens. Matter **26**, 123202 (2014).

[17] X. Zhou, G.-L. Chua, N. Singh, and A. O. Adeyeye, Large area artificial spin ice and Anti-spin ice Ni80Fe20 structures: Static and dynamic behavior, Adv. Funct. Mater. **26**, 1437 (2016).

[18] S. Mamica, X. Zhou, A. Adeyeye, M. Krawczyk, and G. Gubbiotti, Spin-wave dynamics in artificial anti-spin-ice systems: Experimental and theoretical investigations, Phys. Rev. B **98**, 054405 (2018).

[19] S. Gliga, A. Kákay, R. Hertel, and O. G. Heinonen, Spectral analysis of topological defects in an artificial spin-ice lattice, Phys. Rev. Lett. **110**, 117205 (2013).

[20] R. Baillou, M. Terkel, C. Nisoli, and P. Tierno, Emergent charge crystallization and frustration in a particle anti-spin ice, Nat. Commun. **17**, 11152 (2026).

[21] M. Madami, S. Tacchi, G. Gubbiotti, G. Carlotti, J. Ding, A. O. Adeyeye, J. W. Klos, and M. Krawczyk, Spin wave dispersion in permalloy antidot array with alternating holes diameter, IEEE Trans. Magn. **49**, 3093 (2013).

[22] Q. Wang, L. Jin, X. Tang, F. Bai, H. Zhang, and Z. Zhong, Micromagnetic simulation of the dynamic susceptibility spectra of antidot array films with two sublattices, IEEE Trans. Magn. **48**, 3246 (2012).

[23] E. Iacocca, S. Gliga, and O. G. Heinonen, Tailoring spin-wave channels in a reconfigurable artificial spin ice, Phys. Rev. Appl. **13**, 044047 (2020).

[24] E. K. Semenova and D. V. Berkov, Spin wave propagation through an antidot lattice and a concept of a tunable magnonic filter, J. Appl. Phys. **114**, 013905 (2013).

[25] A. O. Adeyeye and N. Singh, Large area patterned magnetic nanostructures, J. Phys. Appl. Phys. **41**, 153001 (2008).

[26] G. Carlotti and G. Gubbiotti, Magnetic properties of layered nanostructures studied by means of Brillouin light scattering and the surface magneto-optical Kerr effect, J. Phys. Condens. Matter **14**, 8199 (2002).

[27] J. R. Sandercock, Trends in brillouin scattering: studies of opaque materials, supported films, and central, in Light Scattering in Solids III: Recent Resultmodes, in *Light Scattering in Solids III: Recent Results*, edited by M. Cardona and G. Güntherodt (Springer, Berlin, Heidelberg, 1982), pp. 173–206.

[28] A. Vansteenkiste, J. Leliaert, M. Dvornik, M. Helsen, F. Garcia-Sanchez, and B. Van Waeyenberge, The design and verification of MuMax3, AIP Adv. **4**, 107133 (2014).

[29] D. Kumar, O. Dmytriiev, S. Ponraj, and A. Barman, Numerical calculation of spin wave dispersions in magnetic nanostructures, J. Phys. Appl. Phys. **45**, 015001 (2011).

[30] R. P. Cowburn, A. O. Adeyeye, and J. A. C. Bland, Magnetic domain formation in lithographically defined antidot Permalloy arrays, Appl. Phys. Lett. **70**, 2309 (1997).

[31] C. C. Wang, A. O. Adeyeye, and N. Singh, Magnetic antidot nanostructures: Effect of lattice geometry, Nanotechnology **17**, 1629 (2006).

[32] W. F. Brown, Virtues and weaknesses of the domain concept, Rev. Mod. Phys. **17**, 15 (1945).

[33] D. Givord, M. Rossignol, and V. M. T. S. Barthem, The physics of coercivity, J. Magn. Magn. Mater. **258–259**, 1 (2003).